INORGANIC CHEMISTRY FRONTIERS

RESEARCH ARTICLE

View Article Online
View Journal | View Issue

Cite this: *Inorg. Chem. Front.*, 2024, **11**, 1087

Harnessing ligand design to develop primary and self-calibrated luminescent thermometers with field-induced single ion magnet behaviour in Dy^{3+} complexes†

Julio Corredoira-Vázquez, [a,b] Cristina González-Barreira, [a] Ana M. García-Deibe, [a] Jesús Sanmartín-Matalobos, [a,c] Miguel A. Hernández-Rodríguez, ‡[b] Carlos D. S. Brites, [b] Luís D. Carlos *[b] and Matilde Fondo *[a]

Novel complexes {[Dy(L^{N6en})$(OAc)_2$](NO_3)}·$2H_2O$ (**1**·$2H_2O$) and {[Dy(L^{N6prop})$(OAc)_2$](NO_3)}·$CHCl_3$ (**2**·$CHCl_3$), containing partially flexible symmetric N_6 macrocycles, are reported. We explore the influence of the spacer length between two symmetrical N_3 rigid moieties of the ligand on their structural, magnetic, and luminescence properties. Crystallographic analysis reveals the presence of Dy^{3+} ions in distorted tetradecahedral (**1**·$2H_2O$) or bicapped square antiprism (**2**·$CHCl_3$) environments. This underscores the increased flexibility of the L^{N6prop} ligand, resulting in greater distortion of the N_6 macrocycle plane. Both complexes exhibit single-molecule magnet behaviour under an optimal field of 2000 Oe, with **2**·$CHCl_3$ displaying the highest U_{eff} value of 127 K, despite its less planar N_6 macrocycle. Luminescence measurements indicate that the ratio between the integrated intensity of the ligands and that of the the Dy^{3+} $^4F_{9/2} \rightarrow {}^6H_{13/2}$ transition can define secondary luminescent thermometers. Maximum relative thermal sensitivity values of 2.3 (**1**·$2H_2O$) and 5.1% K^{-1} (**2**·$CHCl_3$) are achieved. Furthermore, deconvolution of the $^4F_{9/2} \rightarrow {}^6H_{15/2}$ transition in **2**·$CHCl_3$ supports the previous determination of the energy barrier for magnetic relaxation. This permits the demonstration of the first example of a Dy^{3+} primary luminescent thermometer based on two thermally coupled Kramer's doublets of the $^4F_{9/2}$ level. Remarkably, **2**·$CHCl_3$ is also the first self-calibrated luminescent thermometer with magnetic relaxation operating within the 86–211 K range, showcasing its potential in precise temperature sensing applications.

Received 16th November 2023,
Accepted 26th December 2023

DOI: 10.1039/d3qi02374e

rsc.li/frontiers-inorganic

Introduction

Lanthanoid metal ions intrinsically have unique properties that make them particularly attractive for their use in luminescent materials and single-molecule magnets (SMMs).[1] Thus, they show marked single-ion anisotropy due to the combined contributions from strong spin–orbit coupling and the crystal field effect, which is much weaker but critical from the point of view of SMM attributes.[2] In fact, according to Long's theory[3] the axial arrangement of negatively charged donors around oblate lanthanoid ions, such as Dy^{3+}, is the most efficient way to generate high-performance SMMs, with record blocking temperatures of up to 80 K.[4] These molecular magnetic nanomaterials show great potential in magnetic storage, as they would allow data banking and processing at unprecedented speeds.[5]

Lanthanoid ions also exhibit unique luminescent properties due to their f–f electronic transitions, namely in the trivalent state (Ln^{3+}).[6] This has led to the development of luminescent molecular materials with applications in disparate fields, including bioimaging,[7] chemical sensing,[8] and optical thermometry.[9] From a theoretical perspective, combining luminescence and molecular magnet properties provides a powerful tool for understanding magnetic behaviour. High-resolution emission spectra of Ln^{3+} complexes reveal the

[a]*Departamento de Química Inorgánica, Facultade de Química, Universidade de Santiago de Compostela, 15782 Santiago de Compostela, Spain. E-mail: matilde.fondo@usc.es*
[b]*Phantom-g, CICECO – Aveiro Institute of Materials, Department of Physics, University of Aveiro, 3810-193 – Aveiro, Portugal. E-mail: lcarlos@ua.pt*
[c]*Institute of Materials (iMATUS), Universidade de Santiago de Compostela, 15782 Santiago de Compostela, Spain*

†Electronic supplementary information (ESI) available: Structural, magnetic, photoluminescence and thermometric characterization. CCDC 2238908 and 2238909. For ESI and crystallographic data in CIF or other electronic format see DOI: https://doi.org/10.1039/d3qi02374e

‡Current address: Departamento de Física, Universidad de La Laguna, Apdo. Correos 456, E-38200 San Cristóbal de La Laguna, Santa Cruz de Tenerife, Spain.

energy of different electronic states, which directly correlates with the energy barrier for magnetization reversal.[10]

In addition to its theoretical significance, the combination of these two properties holds substantial practical promise. It offers a viable solution to a significant challenge faced in the integration of molecular magnets into next-generation data storage devices – temperature control.[11] Accordingly, SMMs could function as luminescent thermometers, enabling self-monitoring of temperature in these nanomaterials.[12,13] Currently, there are several examples of mono-, di-, or homopolynuclear Nd^{3+},[14] Dy^{3+},[12,15–20] Tb^{3+},[21] Ho^{3+},[22] or Yb^{3+} complexes,[23–25] as well as heteronuclear $Yb^{3+}Co^{3+}$,[26,27] $Dy^{3+}Co^{3+}$,[28,29] or $Dy^{3+}Eu^{3+}$ compounds,[30] in addition to some diluted $Ln^{3+}Y^{3+}$ complexes[31,32] that exhibit both slow relaxation of magnetization and luminescence thermometry (Table 1).

Exploring the intricate interplay of factors that jointly affect both properties is a research topic still in its infancy.

Table 1 Excitation wavelength (λ), temperature range (ΔT), maximum relative sensitivity (S_m), and corresponding temperature (T_m) of the Ln^{3+}-based thermometers with slow relaxation of the magnetization reported so far

Ln^{3+}-SMM thermometer	U_{eff} (K)/H_{dc} (kOe)	Thermometric parameter	λ (nm)	ΔT (K)	S_m (% K^{-1})	T_m (K)	Ref.
$[Nd(TTA)_3(MeOH)_2]$	19.7/1.0	Intensity ratio	392	75–300	0.2[a]	75	14
			360	10–300	0.02[a]	125	
[Dy(bbpen)Cl]	942.4/0		312	12–300	0.3[b]	255	18
$[Dy_4(H_3L^{1,1,4})_2(OAc)_6]\cdot CH_3OH$	39.7/0		358	11–295	1.6[c]	295	17
$[Dy(acac)_3(H_2O)_2]\cdot H_2O$	137/0		364	5–290	5.4[b]	33	16
[Dy(acac)$_3$(PyAm)]	Not Orbach/1.4		328	12–323	2.0[b]	12	15
[Dy(acac)$_3$(PmAm)]	Not Orbach/0		328	12–340	0.8[b]	82	
[Dy(acac)$_3$(bpm)]	309/0		330	30–140	1.5[b]	70	19
$[Dy_2(bpm)(tfac)_6]$	Not Orbach/0		405	5.4–85.5	1.8[d]	5.4	12
			330	90–300	0.5[d]	90	
			330	298–398	3.3[c]	298	
[Dy(tba)$_3$phen]	136.8/0		329	10–50	1.1[b]	50	20
$[DyCo(CN)_6(bpyO_2)_2(H_2O)_3]\cdot 4H_2O$	86.5/1.0		375	11–200	1.8[b]	70	28
					0.2[e]	90	
$\{[Dy_4Co_4(CN)_{24}(4\text{-benpyo})_{17}(H_2O)]\ 7H_2O\}_n$	Not Orbach/2.0		464	16–350	2.3[f]	240	29
$\{(NEt_4)_2[(Ph_4Si_4O_8)_2Dy_{0.87}Eu_{3.12}(NO_3)_6(EtOH)(MeCN)_2]\}\cdot 4MeCN$	16.3/1.0		590/612	293–373	1.2[g]	293	30
$\{[Tb(H_2O)_2][Co(CN)_6]\cdot 2.7H_2O\}$@Y	Not Orbach/2.0		320	8–78	2.6[h]	18.3	31
$\{Tb[Co(CN)_6]\}$	854/3.0		310	6–42	5.3[h]	15.9	
$\{Tb[Co(CN)_6]\}$@Y	859/3.0			6–96	5.4[h]	14.7	
$\{[Ho(4\text{-pyridone})_4(H_2O)_2][Co(CN)_6]\}$@Y	Not Orbach/0.15		370	25–140	6.9[i]	28	22
				60–195	5.8[j]	58	
$\{[Ho(4\text{-pyridone})_4(H_2O)_2][Rh(CN)_6]\}$@Y	Not Orbach/0.1			25–130	2.7[i]	42	
				55–205	4.5[j]	69	
$\{[Ho(4\text{-pyridone})_4(H_2O)_2][Ir(CN)_6]\}$@Y	Not Orbach/0.1			35–144	4.6[i]	37	
				70–197	5.3[j]	61	
$[Yb_2(valdien)_2(NO_3)_2]$	65.6 /1.0		390	80–320	1.1[k]	130	23
$[Yb(H_3L^{1,1,4})]\cdot 2MeOH$	Not Orbach/1.6		360	25–300	0.2[k]	300	24
$[Yb(TPPO)_3(NCS)_3]$	nr/1.5		320	10–300	1.5[k]	150	25
$[Yb(TPPO)_3(NCSe)_3]$	nr/1.5		360	10–300	1.7[k]	150	
$\{(H_5O_2)_2(H)[Yb(hmpa)_4][Co(CN)_6]_2\}$	Not Orbach/1.0		320	50–175	4.6[k]	50	26
$[YbCo(CN)_6(bpyO_2)_2(H_2O)_3]$	Not Orbach /1.25		315	125–275	0.1[k]	180	27
$[Tb_2(bpm)(acac)_6]$	34.3/1.0	Lifetime	350	83–283	4.9[l]	250	21
$[Tb_2(bpm)(tfac)_6]$	nr		330	83–413	5.9[l]	300	
$[Tb_2(bpm)(hfac)_6(H_2O)_2]$	nr		350	83–323	2.4[l]	320	
$[NaDy_{0.02}Y_{0.98}(\mu_2\text{-L})_4]_n$	68.0/0	Single intensity band	350	80–300	0.8[m]	300	32

TTA = 4,4,4-trifluoro-1-(2-thienyl)-1,3-butanedione; H_2bbpen = H_2bbpen=*N*,*N*′-bis(2-hydroxybenzyl)-*N*,*N*′-bis(2-methylpyridyl)ethyl-enedi-amine; $H_3L^{1,1,4}$ = N_4O_3 aminophenol; $acac^-$ = acetylacetonate; PyAm = 2-amidinopyridine; PmAm = 2-amidinopyrimidine; bpm = 2,2′-bipyrimidine; $tfac^-$ = 1,1,1-trifluoroacetylacetonate; tba^- = thiobenzoate; phen = phenantroline; $bpyO_2$ = 2,2′-dipyridyl *N*,*N*′-dioxide; 4-benpyo = 4-benzyloxy-pyridine *N*-oxide; HL = 8-hydroxyquinoline; $hfac^-$ = hexafluoroacetylacetonate; H_2valdien = *N*1,*N*3-bis(3-methoxysalicylidene)diethylenetriamine; TPPO = triphenylphosphine oxide; hmpa = hexamethylphosphoramide. [a] Two components of the $^4F_{3/2} \rightarrow {}^4I_{9/2}$ transition. [b] Two components of the $^4F_{9/2} \rightarrow {}^6H_{13/2}$ transition. [c] Ligand ($T_1 \rightarrow S_0$) and Dy^{3+} ($^4F_{9/2} \rightarrow {}^6H_{13/2}$) emission bands. [d] Two spectral ranges of the $^4F_{9/2} \rightarrow {}^6H_{15/2}$ transition. [e] Two components of the $^4F_{9/2} \rightarrow {}^6H_{15/2}$ transition. [f] Ligand and Dy^{3+}-related emission bands. [g] $^5D_0 \rightarrow {}^7F_4$ transition upon 590 ($^7F_1 \rightarrow {}^5D_0$) and 612 nm ($^7F_2 \rightarrow {}^5D_0$) excitations. [h] Two spectral ranges of the $^5D_4 \rightarrow {}^7F_6$ transition. [i] $^5I_8 \rightarrow {}^5F_1$ (446 nm) and $^5I_8 \rightarrow {}^5G_6$ (456 nm). [j] $^5I_8 \rightarrow {}^5F_1$ (446 nm) and $^5I_8 \rightarrow {}^5G_6$ (459 nm). [k] Two spectral ranges ascribed to the $^2F_{5/2} \rightarrow {}^2H_{7/2}$ transition. [l] S_r obtained from the fitting procedure of the lifetime values according to a Mott–Seitz model. [m] Ligand band.

Therefore, in this work, leveraging our experience in luminescence thermometry of Ln^{3+} complexes with slow relaxation of magnetization,[16,17,24,27,28] we investigate the impact of the aliphatic chain as a spacer between the N_3 units of a symmetric hexadentate N_6 ligand on the magnetic and thermometric properties of its Dy^{3+} derivatives. Moreover, we investigate the temperature determination using both secondary (requiring previous calibration) and primary (not requiring previous calibration) luminescence thermometry, comparing the performance of both approaches and discussing their ability to accomplish self-calibration of the luminescent thermometers.

Results and discussion

Synthetic procedures

The macrocyclic complexes $\{[Dy(L^{N6en})(OAc)_2](NO_3)\}\cdot 2H_2O$ (**1**·2H$_2$O) and $\{[Dy(L^{N6prop})(OAc)_2](NO_3)\}\cdot CHCl_3$ (**2**·CHCl$_3$) were obtained in a classical template synthesis, from the reaction of $Dy(OAc)_3\cdot 4H_2O$, $Dy(NO_3)_3\cdot 6H_2O$, ethylene- or propylendiamine and 2,6-pyridinedicarboxaldehyde in adequate molar ratios, as shown in Scheme 1. This procedure is similar to that previously described for the isolation of $\{[Dy(L^{N6en})(NO_3)_2](NO_3)\}$.[33] In both cases, the complexes were obtained by refluxing the mixtures in methanol. The concentration of the reaction solutions leads to the isolation of oils, the recrystallisation of which in $CHCl_3$ layered with diethyl ether yields **1**·2H$_2$O and **2**·CHCl$_3$ as single crystals.

These were characterized not only by X-ray diffraction studies but also by elemental analysis and IR spectroscopy (Fig. S1†). Thus, the IR spectra of both compounds show characteristic bands of the iminic and pyridinic C=N bonds at *ca.* 1660 and 1590 cm^{-1}, respectively.[34] In addition, both complexes show typical bands that can be attributed to the acetate ligands at *ca.* 1540 and 1450 cm^{-1},[35] as well as a strong band at *ca.* 1330 cm^{-1}, in agreement with the presence of the nitrate counterion.[35,36]

X-ray diffraction studies

Fig. S2† and Fig. 1 show ellipsoid diagrams for complexes **1**·2H$_2$O and **2**·CHCl$_3$, respectively, and their main distances

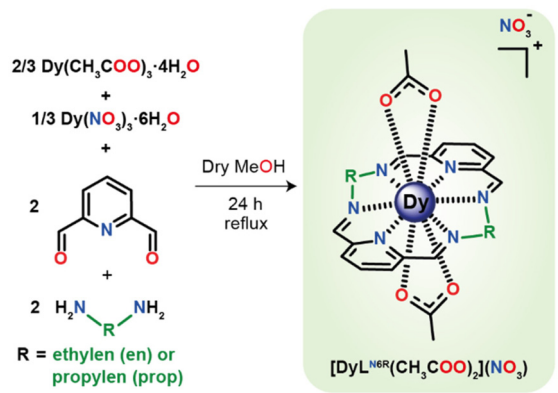

Scheme 1 Synthetic route for the isolation of $\{[Dy(L^{N6en})(OAc)_2](NO_3)\}$ and $\{[Dy(L^{N6prop})(OAc)_2](NO_3)\}$. Solvate molecules are omitted for clarity.

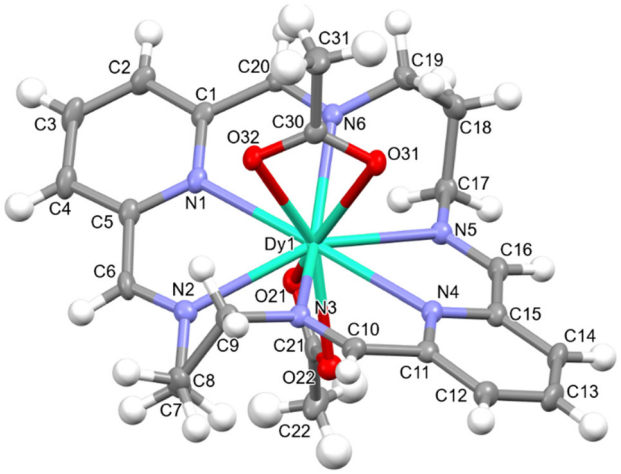

Fig. 1 Ellipsoid diagram (50% probability) for the cation $[Dy(L^{N6prop})(OAc)_2]^+$ in **2**·CHCl$_3$.

and angles around the Dy^{3+} ions are summarised in Table S1.† Both complexes are quite similar to the previously reported $\{[Dy(L^{N6cet})(OAc)_2](OAc)\}\cdot 9H_2O$, where L^{N6acet} is the Schiff base resulting from the condensation of acetophenone and ethylendiamine,[37] and to $\{[Dy(L^{N6en})(NO_3)_2](BPh_4)\}$.[33]

1·2H$_2$O and **2**·CHCl$_3$ also show many similarities between them, and for this reason, they will be described together. Their unit cell contains $[Dy(L^{N6x})(OAc)_2]^+$ (x = en or prop) cations, NO_3^- anions, and different solvates (two water molecules per complex in **1**·2H$_2$O and one $CHCl_3$ molecule per complex in **2**·CHCl$_3$). In the $[Dy(L^{N6x})(OAc)_2]^+$ cations, the semi-rigid Schiff base ligands L^{N6en} or L^{N6prop} act as neutral hexadentates, occupying the equatorial plane in the vicinity of Dy^{3+}. The pyridine N-atoms are the ones that deviate the least from the mean calculated N_6 plane, and the deviation is even smaller for **1**·2H$_2$O than for **2**·CHCl$_3$, with the Dy^{3+} ion standing out very little from this theoretical plane (Table S2†). Nevertheless, the imine nitrogen atoms protrude significantly from this plane. Accordingly, these N-atoms are *ca.* 0.5 Å above or below the plane (2 above and 2 below) for **1**·2H$_2$O, and *ca.* 0.73 Å for **2**·CHCl$_3$, indicating that the longer aliphatic chain favours a greater distortion of this equatorial plane formed by the N_6 donor, as could be expected.

The coordination sphere of the Dy^{3+} ion is fulfilled by two acetate anions, acting as bidentate chelate donors, which leads to coordination number 10 around Dy^{3+}, with a N_6O_4 environment. The calculations of the grade of distortion of the DyN_6O_4 core relative to an ideal polyhedron of ten vertexes with the SHAPE program[38] reveal a largely distorted geometry, between a tetradecahedron (as in the related $\{[Dy(L^{N6en})(NO_3)_2](BPh_4)\}$[33]) and a staggered dodecahedron for **1**·2H$_2$O, and between a bicapped square antiprism and a sphenocorona for **2**·CHCl$_3$ (Table S3†). Accordingly, the length of the spacer between the imine moieties has a profound impact on the geometry of the complex, which will obviously have significant repercussions for the magnetic and luminescence properties.

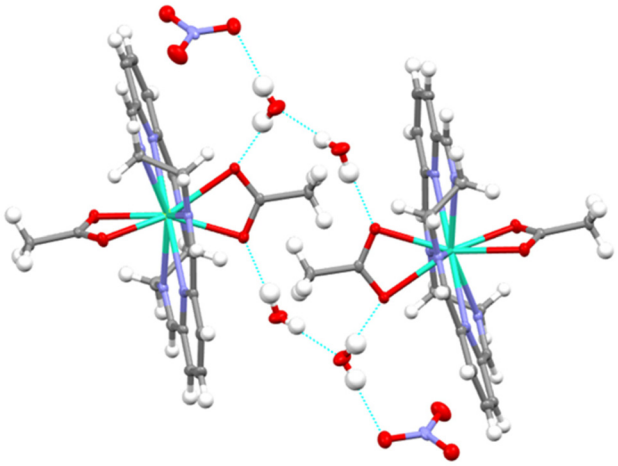

Fig. 2 Hydrogen bond scheme for $1{\cdot}2H_2O$, showing the pseudo-dimer arrangement.

The main angles and distances of the Dy^{3+} ion (Table S1†) are comparable with those previously reported for this kind of compound,[33,37] and do not deserve further consideration.

Finally, the mononuclear units $[Dy(L^{N6en})(OAc)_2]^+$ in $1{\cdot}2H_2O$ establish hydrogen bonds with the water solvates, in such a way that pseudodimers are formed (Fig. 2), with an intermolecular Dy···Dy distance of 8.9404(6) Å. In the case of $2{\cdot}CH_3Cl$, the chloroform solvate seems to be held in the cell by weaker interactions, and no hydrogen bonds are observed, but a quite strong interaction between Cl12 and O2, with a distance of 2.82 Å, is observed (Fig. S3†). These interactions lead to longer intermolecular Dy···Dy distances of 9.8809(6) Å.

In addition, powder X-ray diffraction measures for raw samples of $1{\cdot}2H_2O$ and $2{\cdot}CHCl_3$ were performed (Fig. S4†). These studies show that the isolated products and the solved single crystals are the same complexes and that they have been obtained with high purity, given that no other peaks can be observed in the experimental diffractograms.

Magnetic properties

Direct-current (dc) magnetic susceptibility measurements were recorded for $1{\cdot}2H_2O$ and $2{\cdot}CHCl_3$ as a function of the temperature. The graphs of $\chi_M T$ *vs.* T are shown in Fig. 3. The $\chi_M T$ values for the complexes at 300 K are 14.2 $cm^3\ mol^{-1}$ K in both cases, which are very close to the expected value for one uncoupled Dy^{3+} ion at room temperature (14.17 $cm^3\ mol^{-1}$ K).[39] The experimental curves continuously decrease until 2 K, reaching $\chi_M T$ values close to 10.5 $cm^3\ mol^{-1}$ K. This drop in the curves can be mainly ascribed to thermal depopulation of the excited Kramer's doublets (KDs), which arises from the split of the ground term by crystal field effects.

The magnetic field dependence of the reduced magnetisation at 2 K at the maximum applied field of 7 T is $5.8N\mu_B$ for $1{\cdot}2H_2O$ and $5.3N\mu_B$ for $2{\cdot}CHCl_3$ (Fig. 3). These values are lower than the theoretical saturation characteristic of an isolated Dy^{3+} ion ($10N\mu_B$), but quite close to the value of $5N\mu_B$ for a highly anisotropic Dy^{3+} ion with an Ising-like ground doublet.[2]

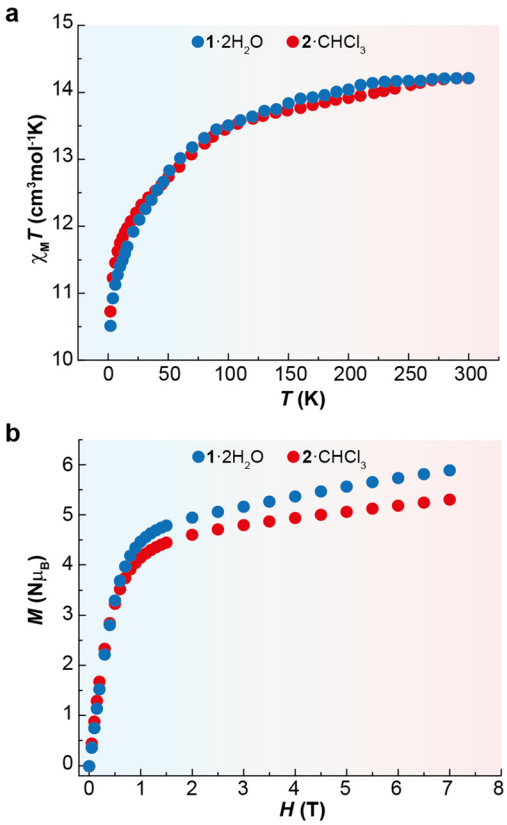

Fig. 3 (a) $\chi_M T$ *vs.* T and (b) $M/N\mu_B$ *vs.* H at 2 K for $1{\cdot}2H_2O$ and $2{\cdot}CHCl_3$.

The dynamic magnetic properties of the two mononuclear complexes were also studied, but none of the compounds show out-of-phase peaks of the susceptibility (χ''_M) as a function of the temperature or the frequency above 2 K, as occurs in $\{[Dy(L^{N6cet})(OAc)_2][OAc]\}{\cdot}9H_2O$,[37] and $\{[Dy(L^{N6en})(NO_3)_2](BPh_4)\}$.[33] This can be a consequence of the quantum tunnelling of the magnetization (QTM).

Accordingly, the alternating-current (ac) data were newly recorded in the presence of an optimum field of 2000 Oe (Fig. S5†), and now χ''_M for $1{\cdot}2H_2O$ and $2{\cdot}CHCl_3$ shows frequency and temperature dependence, with clear peaks (Fig. 4 and Fig. S6†), in agreement with single ion magnet (SIM) behaviour. Besides, the Cole–Cole plots (Fig. S7†) display curves with a wider distribution of the relaxation times for $1{\cdot}2H_2O$ (α parameter in the range 0.45–0.53) than for $2{\cdot}CHCl_3$ (α values in the range 0.33–0.29). The relaxation dynamics were examined by the temperature dependence of the relaxation time (Fig. 5). The data deviate from linearity, indicating that the curve cannot be adequately reproduced by a simple Orbach model, as anticipated given the α parameter values. Hence, we have tried to fit these plots considering all the possible relaxation processes (Orbach, Raman, direct, and QTM), according to eqn (1), individually or grouped.

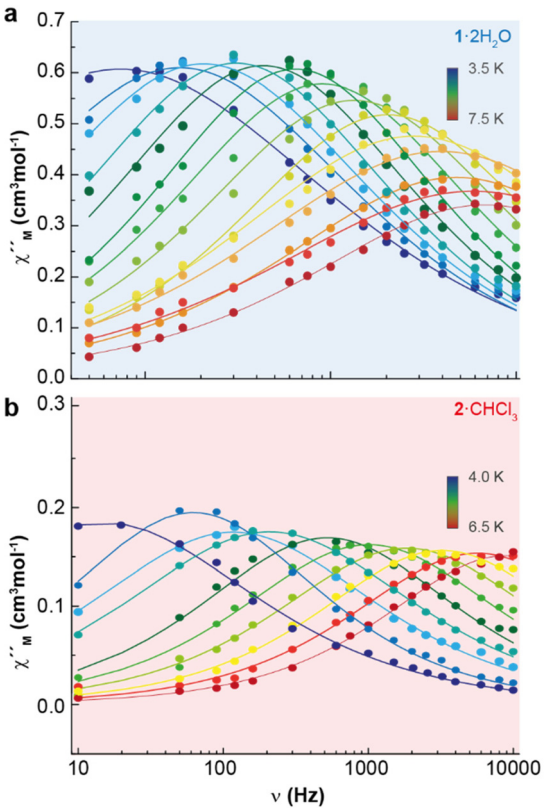

Fig. 4 Frequency dependence of χ''_M for **1**·2H_2O (a) and **2**·$CHCl_3$ (b) in a dc-applied field of 2000 Oe at different temperatures.

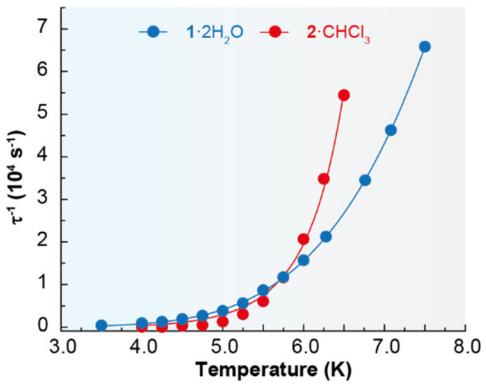

Fig. 5 Dependence of the relaxation time with temperature for **1**·2H_2O and **2**·$CHCl_3$ in a dc applied field of 2000 Oe. The blue and red solid lines account for the best fit ($r^2 > 0.99$) considering Orbach plus Raman relaxation processes.

$$\tau^{-1} = \tau_0{}^{-1} e^{-U_{eff}/k_B T} + CT^n + AT + \tau_{QTM}{}^{-1} \quad (1)$$

The best fits of the data are obtained in both cases considering Orbach and Raman relaxation processes, and these render the parameters U_{eff} = 46.3(1) K (32.2 ± 0.7 cm^{-1}), τ_0 = 4.0(2) × 10^{-8} s, C = 0.4(1) s^{-1} K^{-n}, and n = 5.2(5) for **1**·2H_2O, and U_{eff} = 127.0(4) K (88.3 ± 0.2 cm^{-1}), τ_0 = 1.3(1) × 10^{-13} s, C = 2.2(6) × 10^{-3} s^{-1} K^{-n}, and n = 8.7(1) for **2**·$CHCl_3$.

The energy barrier between the ground and first excited state for **2**·$CHCl_3$ was also calculated by luminescence spectroscopy (100.2 cm^{-1}, *vide infra*), and, accordingly, these studies support the thermally activated Orbach relaxation pathway. However, it is not possible to perform these spectroscopic calculations for **1**·2H_2O, as detailed below, but its barrier is similar to the one obtained for {[Dy(L^{N6en})(NO_3)$_2$](BPh_4)} (37.8 K).[33] In spite of this, the relaxation dynamics of **1**·2H_2O were also analysed excluding the Orbach mechanism, and the data can be simply fitted with a Raman process (Fig. S8†), rendering the values C = 0.13(2) s^{-1} K^{-n} and n = 6.5 (1), comparable with those observed for {[Dy(L^{N6en})(NO_3)$_2$](BPh_4)}. Nevertheless, multiple attempts to fit the τ^{-1} *vs.* T curve for **2**·$CHCl_3$ without considering the Orbach process were unsuccessful, which also supports the proposed Orbach plus Raman relaxation pathways. Comparing the energy barriers of **1**·2H_2O, **2**·$CHCl_3$ and the related {[Dy(L^{N6en})(NO_3)$_2$](BPh_4)} complex reveals that the exchange between bidentate chelate nitrate and acetate ligands has minimal impact on U_{eff}, while the chain length between the N_3 entities of N_6 macrocyclic ligands significantly affects magnetic relaxation. This observation suggests that a greater barrier should be expected for **1**·2H_2O and {[Dy(L^{N6en})(NO_3)$_2$](BPh_4)}, due to their less distorted N_6 planes, and geometries closer to a pseudo-hexagonal bipyramid. However, U_{eff} is unexpectedly higher for **2**·$CHCl_3$. Accordingly, it seems that the less semirigid ligand induces the highest energy barrier for the spin reversal. Additionally, as anticipated,[40] the nature of the counteranion appears to have no influence on U_{eff}.

Photoluminescence

Excitation spectra for both compounds were recorded while monitoring the $^4F_{9/2} \rightarrow {}^6H_{13/2}$ transition at 570 nm, revealing both sharp and broadband features (Fig. S9†). These features were assigned to transitions from the Dy^{3+} ions and organic ligands, respectively. The presence of the latter contribution indicates ligand-sensitized emission.

Fig. 6 depicts the temperature dependence of the emission spectra of **1**·2H_2O and **2**·$CHCl_3$, recorded using excitation wavelengths of 324 nm and 326 nm, respectively, in agreement with the maxima observed in the excitation spectrum. We observe the characteristic Dy^{3+} $^4F_{9/2} \rightarrow {}^6H_{11/2,\ 13/2,\ 15/2}$ *intra*-4f transitions within the visible spectral region. At all examined temperatures, the emission spectra exhibited a broad band in the UV-visible spectral region, attributed to the ligands. This band is notably more intense in **1**·2H_2O than in **2**·$CHCl_3$. This behaviour has been previously observed for Er^{3+} derivatives with the same macrocyclic ligands.[41] Moreover, the energy of the triplet state for both ligands was estimated, and they do not differ significantly in energy (~25 063 cm^{-1}).[41]

However, despite having the same energy for the donor state, minor structural differences may result in shifting donor–acceptor distances, *i.e.* the centroid of the ligand excited state (T_1 or S_1) to the Ln^{3+} ion. A shorter distance, in turn, may lead to a faster energy transfer rate.[42] For instance, it is known that the excited states of the ligand are localized near

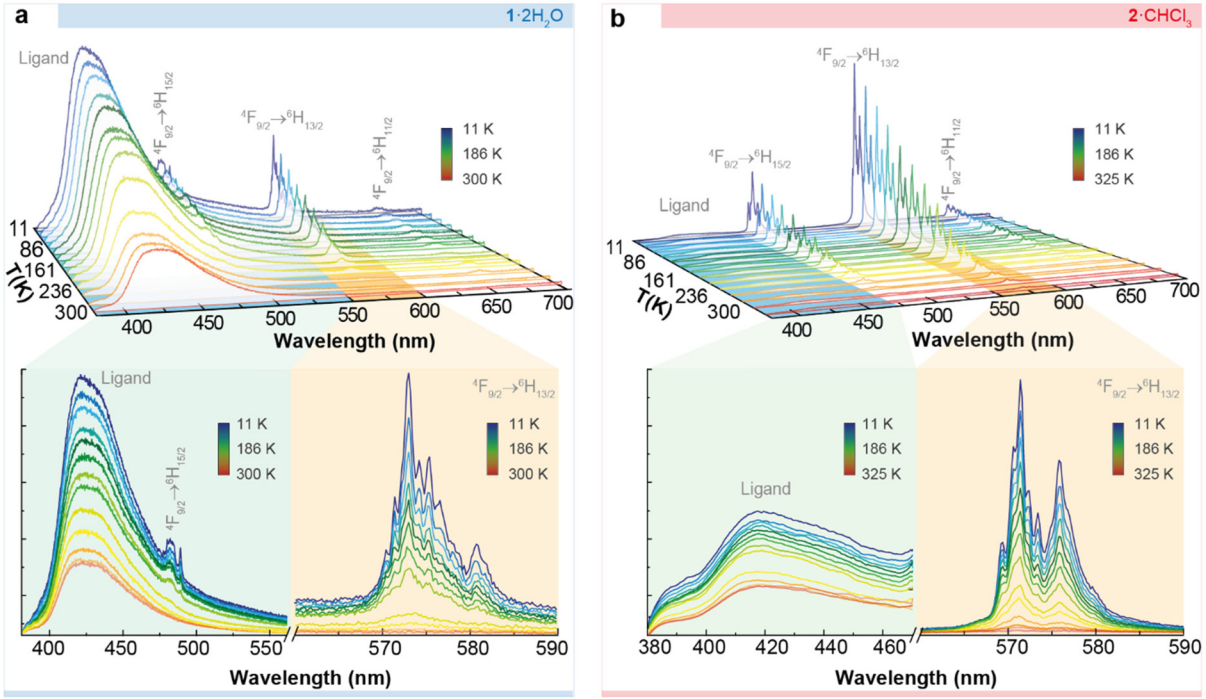

Fig. 6 Temperature dependence (11–350 K) of the emission spectra of (a) **1**·2H_2O (excited at 324 nm) and (b) **2**·$CHCl_3$ (excited at 326 nm). The insets depict enlarged views of the ligand and Dy^{3+} f–f transitions.

an electronic delocalization structure, as discussed elsewhere.[42–46] This may imply variations in the energy transfer rates from the excited states (in this case, the T_1) of the macrocyclic ligand L^{N6en} or L^{N6prop} to Dy^{3+}. Qualitatively, it is clear that the ligand-to-metal energy transfer is more effective in **2**·$CHCl_3$, which can be justified based on structural differences, even when this difference is slight. In **2**·$CHCl_3$, the donor–acceptor distance of the triplet state is shorter (Fig. S10†), leading to higher energy transfer rates and a more efficient "antenna" effect.

For **2**·$CHCl_3$, we deconvoluted the $^4F_{9/2} \rightarrow {}^6H_{15/2}$ transition to extract more detailed information (Fig. S11†). As Dy^{3+} is a Kramer's ion, the maximum crystal field splitting of a level into KDs should be $J + 1/2$. The presence of at least 9 components, exceeding the anticipated 8 KDs for the $^6H_{15/2}$ level (attributed to the low symmetry Dy^{3+} local group), points out that the first excited KD of the $^4F_{9/2}$ level is populated (even at 11 K), resulting in the formation of what is commonly referred to a hot band. The deconvolution permits calculation of the relative energy of each KD, as depicted in Fig. S12.† The results reveal an energy gap between the first two KDs of the $^6H_{15/2}$ ground level of 100.2 ± 0.3 cm^{-1} (referred to as ΔE_1). The energy gap between the first two KDs of the $^4F_{9/2}$ emitting level (referred to as ΔE_2) is 98 ± 0.3 cm^{-1}.

As mentioned above, the value found, 100.2 ± 0.3 cm^{-1}, is similar to but slightly higher than the energy barrier observed in the ac magnetic studies (88.3 ± 0.2 cm^{-1}). Comparable differences between magnetic and luminescent calculated barriers were found for previously reported complexes,[47] thus supporting the interpretation of the magnetic results. On the contrary, for **1**·2H_2O, the overlap between the emissions of the ligands and Dy^{3+} ions precluded the deconvolution (Fig. 6a), and, therefore, the calculation of the energy gaps between m_j states.

Luminescence thermometry

The ratio between the integrated intensity of the ligand (I_L) and that of the dominant Dy^{3+} $^4F_{9/2} \rightarrow {}^6H_{13/2}$ transition (I_F) is defined as the thermometric parameter (Δ) and is used to assess the thermometric properties of **1**·2H_2O and **2**·$CHCl_3$ (Fig. S13 and section 4 of the ESI† for details). The difference in the temperature dependence of I_L and I_F in both complexes underscores the influence of the spacer length between the two symmetrical N_3 rigid moieties of the ligand on the luminescence of these compounds.

Fig. 7 shows the temperature dependence of Δ for both compounds, which exhibits a linear decrease. For **2**·$CHCl_3$, the operating range as a luminescent thermometer encompasses 11–286 K, while for **1**·2H_2O it is narrower (11–211 K). For temperatures higher than 286 and 211 K, respectively, the variations in Δ are of the same order of their uncertainties and, thus, **1**·2H_2O and **2** $CHCl_3$ are out of the thermometric operating range.[48]

The thermometric performance of the two compounds was assessed through the typical figures of merit for luminescent thermometers: S_r and δT[49,50] (Fig. 8 and ESI† for details). Whereas **1**·2H_2O achieves a maximum S_r value of 2.3% K^{-1}, **2**·$CHCl_3$ has 5.1% K^{-1}. The corresponding minimum tempera-

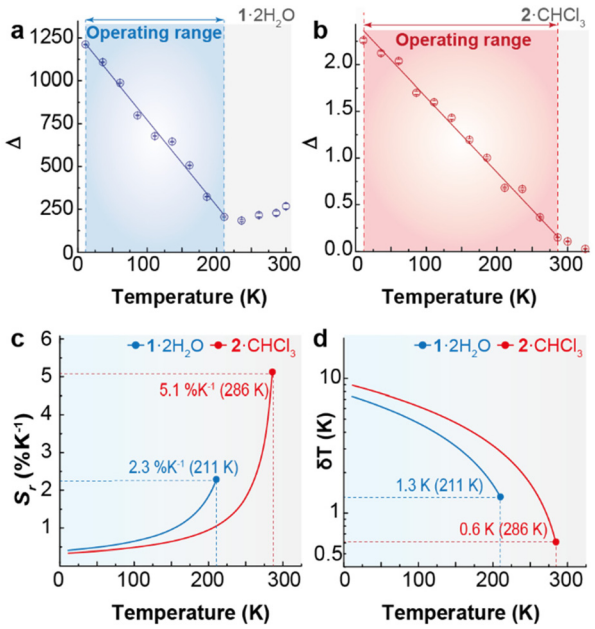

Fig. 7 Temperature dependence of the thermometric parameter (Δ) for (a) **1**·2H_2O and (b) **2**·$CHCl_3$. The lines represent the best linear fits (r^2 > 0.99) to the experimental data (fit details in Table S5†). Temperature dependence of (c) S_r and (d) δT for **1**·2H_2O and **2**·$CHCl_3$.

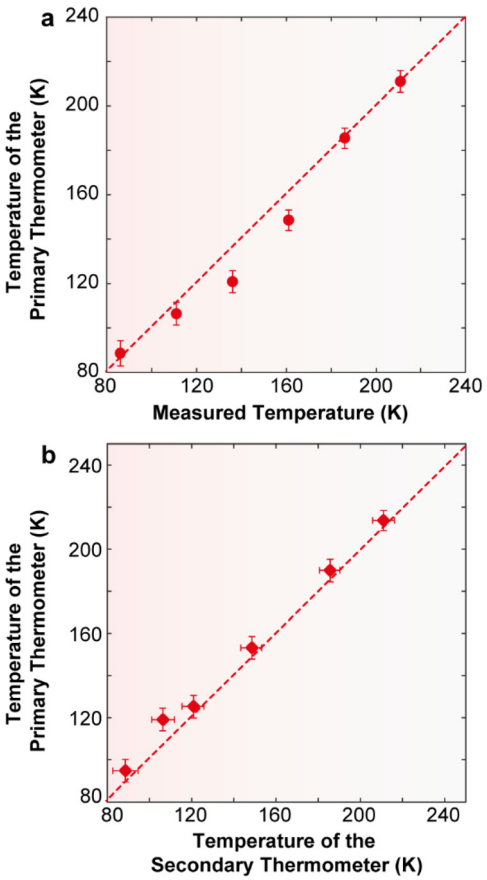

Fig. 8 (a) Comparison between the temperature values measured using a reference silicon thermometer (*y*) and calculated using eqn (2) (*x*) for **2**·$CHCl_3$. The solid line is a guide for the eyes corresponding to $y = x$. The horizontal error bars are the temperature uncertainty on the calculated temperature, calculated using eqn (S10).† The uncertainties in the measured temperature (not represented) are 0.5 K (12–30 K), 0.25 K (30–60 K), and 0.15 K (60–300 K). (b) Dependence of the calibrated temperature (*y*) with the calculated value (*x*). The solid line is a guide for the eyes corresponding to $y = x$. The horizontal and vertical error bars are the temperature uncertainty on the calculated temperature, calculated using eqn (S10) and (S6),† respectively.

ture uncertainty values are 0.1 K and 0.2 K, respectively, at the indicated temperatures.

In addition to the previously discussed intensity ratio between the ligand and the $^4F_{9/2} \rightarrow {}^6H_{13/2}$ transition, the concept of a primary luminescent thermometer can also be applied in **2**·$CHCl_3$. Primary luminescent thermometers eliminate the need for prior calibration procedures, a major advantage in luminescence thermometry.[51] Indeed, **2**·$CHCl_3$ is the first example of a Dy^{3+} primary luminescent thermometer based on the intensity ratio between transitions from the lowest energy state or second lowest energy state of the excited $^4F_{9/2}$ level to the $^6H_{15/2}$ ground state multiplet.[51] The other reported example of a Dy^{3+} primary luminescent thermometer with slow magnetic relaxation operating in the presence of a magnetic field up to 3.6 T is based on the classical Mott–Seitz model.[16]

Beyond Dy^{3+}, primary luminescent thermometers have also been explored in Yb^{3+}/Er^{3+}-doped upconverting materials,[51–53] and Yb^{3+}/Pr^{3+} co-doped fluoride phosphate glasses.[54] This technique uses the ratio between the intensities arising from two thermally coupled levels of the Ln^{3+} ions that are directly related to the absolute temperature, *T*, through a well-established equation:

$$\frac{1}{T} = \frac{1}{T_0} - \frac{k_B}{\Delta E_2} \ln\left(\frac{\Delta'}{\Delta'_0}\right) \quad (2)$$

where k_B is the Boltzmann constant, ΔE_2 is the energy gap between the barycenters of the thermally coupled levels (Fig. S11†), and Δ' is the thermometric parameter ascribed to the two Ln^{3+} thermally coupled KDs of the $^4F_{9/2}$ level, with Δ'_0 being the value at the temperature T_0. Usually ΔE_2 and Δ'_0 are determined independently of the thermal calibration procedure, the first by a deconvolution procedure involving the emission spectra for determining the energy gap value and the second by an extrapolation of Δ' when external heating is negligible.[51]

Taking advantage of the distinct temperature dependence of the deconvolution of the $^4F_{9/2} \rightarrow {}^6H_{15/2}$ transition, the energy gap between the fundamental and first level (hot band) of the $^4F_{9/2}$ state was estimated to be $\Delta E = 98 \pm 0.3$ cm^{-1} (Fig S12†). The excitation source does not induce local discernible temperature increments, ensuring that the Δ'_0 value could be determined for any given temperature value.

To illustrate that **2**·$CHCl_3$ is a luminescent primary thermometer, we begin by plotting $\ln(\Delta')$ *versus* $1/T$ to identify the temperature range for which eqn (2) is valid (*i.e.*, a linear

relation between $\ln(\Delta)$ and $1/T$, Fig. S14†). We conclude that a linear relation is observed for $86 \leq T \leq 211$ K. Thus, we set T_0 = 211 K and Δ'_0 = 0.1477, where T_0 corresponds to the value that minimizes the absolute deviation between the calculated and measured temperatures. Next, we apply eqn (2) and find that the temperature value predicted by the primary thermometer fits well with the temperature determined experimentally by the calibration procedure up to 211 K. The deviation between predicted and measured values can be quantified using the mean absolute deviation, which is 5% for the primary thermometer (Fig. S15†). The S_r and δT for the primary **2**·$CHCl_3$ luminescence thermometer (Fig. S16†) are comparable with those of the secondary thermometer, the best values being 1.8%·K^{-1} and 2 K, respectively, at 86 K.

Additionally, and as an added benefit, in **2**·$CHCl_3$ the primary molecular thermometer can be used to calibrate the secondary one, offering an extra advantage of this compound. Fig. 8b illustrates the calibration of the ratio between the integrated intensity of the ligand and that of the Dy^{3+} $^4F_{9/2} \rightarrow {}^6H_{13/2}$ transition (secondary thermometer) using the temperature calculated using eqn (2) (primary thermometer). Notably, the uncertainty associated with the calculated temperature values is comparable with that of the calibrated temperature. A previous study on a poly(methylmethacrylate) film containing Er^{3+}- and Tm^{3+}-doped upconverting nanoparticles has demonstrated the use of a luminescent primary thermometer based on the Er^{3+} $^2H_{11/2} \rightarrow {}^4I_{15/2}$ and $^4S_{3/2} \rightarrow {}^4I_{15/2}$ transitions to calibrate a secondary thermometer based on the $^1G_4 \rightarrow {}^3H_6$ (Tm^{3+}) and the $^4S_{3/2} \rightarrow {}^4I_{15/2}$ (Er^{3+}) transitions.[55]

Conclusions

The structural features and the magnetic and luminescence properties of mononuclear Dy^{3+} complexes derived from symmetrical N_6 semirigid macrocycles are strongly influenced by the spacer between the two N_3 rigid moieties. This is evident in the different coordination geometries observed for {[Dy(L^{N6en})$(OAc)_2$][NO_3)}·$2H_2O$ (**1**·$2H_2O$) (tetradecahedron) and {[Dy(L^{N6prop})$(OAc)_2$][NO_3)}·$CHCl_3$ (**2**·$CHCl_3$) (bicapped square antiprism). These different environments also impact the magnetic properties of the complexes, which behave as SIMs in the presence of a dc field, with **2**·$CHCl_3$ exhibiting the highest energy barrier.

The luminescence measurements show that the ratio between the integrated intensity of the ligands and that of the Dy^{3+} $^4F_{9/2} \rightarrow {}^6H_{13/2}$ transition can be used to develop secondary luminescent thermometers with maximum relative thermal sensitivity values of 2.3 (**1**·$2H_2O$) and 5.1% K^{-1} (**2**·$CHCl_3$). The minimum temperature uncertainties are, respectively, 1.3 (at 211 K) and 0.6 K (at 286 K). These values are comparable with those already reported for analogous thermographic SIMs (Table 1), and also show the better thermometric characteristics of **2**·$CHCl_3$ with respect to **1**·$2H_2O$.

The deconvolution of the $^4F_{9/2} \rightarrow {}^6H_{15/2}$ transition in **2**·$CHCl_3$ provides further support for the determination of the energy barrier for magnetic relaxation. Moreover, this deconvolution enables the demonstration of the first example of a Dy^{3+} primary luminescent thermometer based on two thermally coupled KDs of the $^4F_{9/2}$ level. Additionally, **2**·$CHCl_3$ is the first self-calibrated luminescent thermometer with magnetic relaxation, operating within the 86–211 K range. The calibration of the luminescent secondary thermometer closely aligns with the calculated temperature of the primary thermometer, with observed uncertainties in calculated temperature values comparable with the calibrated temperatures. As the intensity ratio between the fundamental and first excited KDs of the $^4F_{9/2}$ level and the ground KD of the $^6H_{15/2}$ multiplet is calibrated through eqn (2), it eliminates the need for recurrent calibration procedures whenever the system operates in new conditions. Therefore, **2**·$CHCl_3$ is unique among its class, and it not only contributes to increasing the very small number of SMMs with primary luminescence thermometry, but also represents a significant advancement in the various mechanisms of luminescent thermometers using Dy^{3+} as the emitter.

Experimental

Materials and general methods

All chemical reagents were purchased from commercial sources and used as received without further purification. Elemental analyses of C, H, and N were performed on a Themoscientific Flash Smart analyser. FT-IR spectra were recorded on a Varian FT–IR 670 spectrometer equipped with an attenuated total reflectance (ATR) accessory, in the 500–4000 cm^{-1} range.

Syntheses

The Dy^{3+} complexes were obtained by variation of a method previously reported.[40] The synthesis of {[Dy(L^{N6en})$(OAc)_2$][NO_3)}·$2H_2O$ (**1**·$2H_2O$) exemplifies the procedure.

{[Dy(L^{N6en})$(OAc)_2$][NO_3)}·$2H_2O$ (1·$2H_2O$). 2,6-Pyridinedicarboxaldehyde (0.270 g, 2.000 mmol) was dissolved in dry methanol (40 mL). Then, dysprosium acetate tetrahydrate (0.274 g, 0.667 mmol), dysprosium nitrate hexahydrate (0.152 g, 0.333 mmol), and ethylenediamine (99%, 0.142 mL, 2.100 mmol) were added. After 10 min of stirring, the reaction was refluxed for 24 hours, giving an orange solution. Removing the solvent under vacuum produced an orange oil. The oil was dissolved in chloroform (20 mL), and the solution was layered with diethyl ether and kept in the fridge (at ~5 °C). After a few days, single crystals of [Dy(L^{N6en})$(OAc)_2$][NO_3)·$2H_2O$ (**1**·$2H_2O$) were isolated. The crystals were filtered and dried in air. Yield: 0.366 g (53%). Elemental analysis calcd for $C_{22}H_{28}DyN_7O_9$ (697.00): C 37.91, N 14.07, H 4.05%. Found: C 38.17, N 13.85, H 4.18%. IR (ATR, $\tilde{\nu}$/cm^{-1}): 1534 (COO), 1594 (C=N_{py}), 1659 (C=N_{imine}), 3415 (OH).

{[Dy(L^{N6prop})$(OAc)_2$][NO_3)}·$CHCl_3$ (2·$CHCl_3$). 2,6-Pyridinedicarboxaldehyde (0.270 g, 2.000 mmol) in dry methanol (40 mL), dysprosium acetate tetrahydrate (0.274 g, 0.667 mmol), dysprosium nitrate hexahydrate (0.152 g,

0.333 mmol), 1,3-diaminopropane (99%, 0.178 mL, 2.100 mmol). Recrystallisation as in **1**·2H_2O yielded single crystals of $[Dy(L^{N6prop})(OAc)_2](NO_3)\cdot CHCl_3$ (**2**·$CHCl_3$). Yield: 0.224 g (29%). Elemental analysis calcd for $C_{25}H_{28}DyCl_3N_7O_7$ (808.40): C 37.10, N 12.12, H 3.59%. Found: C 37.33, N 12.16, H 3.71%. IR (ATR, $\tilde{\nu}$/cm^{-1}): 1539 (COO), 1592 (C═N_{py}), 1655 (C═N_{imine}), 3440 (OH).

Single X-ray crystallographic refinement and structure solution

The crystal data and details of refinement are given in Table S4.† Data were collected at 100 K on a Bruker D8 VENTURE PHOTON III-14 diffractometer, employing graphite monochromatised Mo-Kα (λ = 0.71073 Å) radiation. Multi-scan absorption corrections were applied using the SADABS routine.[56] The structure was solved by standard direct methods employing SHELXT,[57] and then refined by full-matrix least-squares techniques on F^2 using SHELXL,[58] from the program package SHELX-2018.[57,58] All atoms different from hydrogen were anisotropically refined, while H atoms were typically included in the structure factor calculations in geometrically idealised positions. However, to reveal the hydrogen bonding scheme, hydrogen atoms belonging to water solvate in **1**·2H_2O were located in the corresponding Fourier map. In this case, they were freely refined.

Powder X-ray diffraction studies

The powder diffractograms for **1**·2H_2O and **2**·$CHCl_3$ were recorded in a Philips diffractometer with a control unity type "PW1710", a vertical goniometer type "PW1820/00" and a generator type "Enraf Nonius FR590", operating at 40 kV and 30 mA, using monochromated Cu-K_α (λ = 1.5418 Å) radiation. A scan was performed in the range $2 < 2\theta < 30°$ with t = 3 s and $\Delta 2\theta$ = 0.02°. LeBail refinement was obtained with the aid of HighScore Plus Version 3.0d.

Magnetic measurements

Magnetic susceptibility dc and ac measurements for microcrystalline samples of **1**·2H_2O and **2**·$CHCl_3$ were carried out with a PPMS Quantum Design susceptometer. The dc magnetic susceptibility data were recorded under a magnetic field of 1000 Oe in the temperature range 2–300 K. Magnetisation measurements at 2.0 K were recorded under magnetic fields ranging from 0 to 70 000 Oe. Diamagnetic corrections were estimated from Pascal's Tables. Alternating current (ac) susceptibility measurements at zero dc field were performed with an oscillating ac field of 3.5 Oe, and ac frequencies of 8000 and 10 000 Hz in the 2–20 K temperature range. ac measurements at 3 K were also recorded under magnetic fields from 250 to 3000 Oe, with an oscillating ac field of 3.5 Oe, and frequencies ranging from 50 to 1500 Hz. New ac data were acquired for **1**·2H_2O and **2**·$CHCl_3$ under a dc field of 2000 Oe, and with frequencies ranging from 50 to 10 000 Hz.

Luminescence measurements

The temperature-dependent emission and excitation spectra of **1**·2H_2O and **2**·$CHCl_3$ (in the solid state) were acquired in a Fluorolog3® spectrofluorometer (FL3-2T, Horiba) with a modular double grating excitation monochromator (fitted with a 1200 grooves per mm grating blazed at 330 nm) and a TRIAX 320 single emission monochromator (fitted with a 1200 grooves per mm grating blazed at 500 nm, reciprocal linear density of 2.6 nm mm^{-1}), coupled with a photomultiplier (R298, Hamamatsu), using the front face acquisition mode. The excitation source was a 450 W Xe arc lamp. The emission spectra were corrected for detection and the optical spectral response of the spectrofluorimeter, and the excitation spectra were corrected for the spectral distribution of the lamp intensity using a photodiode reference detector. The temperature was controlled using a helium-closed cycle cryostat, a vacuum system (4×10^{-4} Pa), and an autotuning temperature controller (Lakeshore 330, Lakeshore) with a resistance heater. The temperature was measured using a silicon diode cryogenic sensor (DT-470-SD, Lakeshore) with accuracies of ±0.5 K (12–30 K), ±0.25 K (30–60 K), and ±0.15 K (60–340 K).

Thermometric measurements

The thermometric performance of the materials was determined using MatLab®. The integrated areas of the transitions and the corresponding errors together with the thermometric parameters were determined as detailed in section 4 in the ESI.† The deconvolution of the $^4F_{9/2} \rightarrow {}^6H_{13/2}$ Dy^{3+} transition was implemented in OriginLab© as detailed in the same section.

Author contributions

Conceptualization: J.C.-V., L.D.C., M.F.; methodology: J.C.-V., C.G.-B, M.A.H.-R., J.S.-M.; validation: L.D.C., M.F.; formal analysis: J.C.-V., A.M.G.-D., C.D.S.B., M.F.; investigation: J.C.-V., C. G.-B; resources: L.D.C., M.F.; visualization: J.C.-V., C.D.S.B.; data curation and supervision: L.D.C., M.F.; writing – original draft preparation: J.C.-V., L.D.C., C.D.S.B, M.F.; writing – review & editing: J.C.-V., C.D.S.B., L.D.C., M.F.; project administration: L.D.C., M.F.; funding acquisition: J. C.-V., L.D.C., M.F. All authors have read and agreed to the published version of the manuscript.

Conflicts of interest

There are no conflicts to declare.

Acknowledgements

This work was developed within the scope of the project CICECO – Aveiro Institute of Materials, UIDB/50011/2020, UIDP/50011/2020, and LA/P/0006/2020, financed by national funds through the FCT/MCTES (PIDDAC). This article is also based upon work from COST Action CA22131, supported by COST (European Cooperation in Science and Technology). The authors acknowledge fruitful discussions with Dr Albano

N. Carneiro Neto (University of Aveiro) concerning ligand-to-metal energy transfer. J. C. V. also thanks Xunta de Galicia for his postdoctoral fellowship (ED481B-2022-068).

References

1 J. Larionova, Y. Guari, S. Sene and G. Félix, in *Handbook on the Physics and Chemistry of Rare Earths*, Elsevier, 2023, DOI: 10.1016/bs.hpcre.2023.10.003.
2 J.-L. Liu, Y.-C. Chen and M.-L. Tong, Symmetry strategies for high performance lanthanide-based single-molecule magnets, *Chem. Soc. Rev.*, 2018, **47**, 2431–2453.
3 J. D. Rinehart and J. R. Long, Exploiting single-ion anisotropy in the design of f-element single-molecule magnets, *Chem. Sci.*, 2011, **2**, 2078–2085.
4 F.-S. Guo, B. M. Day, Y.-C. Chen, M.-L. Tong, A. Mansikkamäki and R. A. Layfield, Magnetic hysteresis up to 80 Kelvin in a dysprosium metallocene single-molecule magnet, *Science*, 2018, **362**, 1400–1403.
5 M. Bałanda and R. Pełka, in *Molecular Magnetic Materials: Concepts and Applications*, ed. B. Sieklucka and D. Pinkowicz, Wiley-VCH, 2017.
6 J.-C. G. Bünzli and C. Piguet, Taking advantage of luminescent lanthanide ions, *Chem. Soc. Rev.*, 2005, **34**, 1048–1077.
7 A. T. Bui, M. Beyler, A. Grichine, A. Duperray, J.-C. Mulatier, Y. Guyot, C. Andraud, R. Tripier, S. Brasselet and O. Maury, Near infrared two photon imaging using a bright cationic Yb(III) bioprobe spontaneously internalized into live cells, *Chem. Commun.*, 2017, **53**, 6005–6008.
8 B. Yan, Lanthanide-functionalized metal–organic framework hybrid systems to create multiple luminescent centers for chemical sensing, *Acc. Chem. Res.*, 2017, **50**, 2789–2798.
9 C. D. S. Brites, S. Balabhadra and L. D. Carlos, Lanthanide-based thermometers: At the cutting-edge of luminescence thermometry, *Adv. Opt. Mater.*, 2019, **7**, 1801239.
10 F. Pointillart, B. le Guennic, O. Cador, O. Maury and L. Ouahab, Lanthanide ion and tetrathiafulvalene-based ligand as a "magic" couple toward luminescence, single molecule magnets, and magnetostructural correlations, *Acc. Chem. Res.*, 2015, **48**, 2834–2842.
11 A. Zabala-Lekuona, J. M. Seco and E. Colacio, Single-molecule magnets: From Mn12-ac to dysprosium metallocenes, a travel in time, *Coord. Chem. Rev.*, 2021, **441**, 213984.
12 D. Errulat, R. Marin, D. A. Gálico, K. L. M. Harriman, A. Pialat, B. Gabidullin, F. Iikawa, O. D. D. Couto, Jr., J. O. Moilanen, E. Hemmer, F. A. Sigoli and M. Murugesu, A luminescent thermometer exhibiting slow relaxation of the magnetization: Toward self-monitored building blocks for next-generation optomagnetic devices, *ACS Cent. Sci.*, 2019, **5**, 1187–1198.
13 R. Marin, G. Brunet and M. Murugesu, Shining new light on multifunctional lanthanide single-molecule magnets, *Angew. Chem., Int. Ed.*, 2021, **60**, 1728–1746.
14 K. Kumar, D. Abe, K. Komori-Orisaku, O. Stefańczyk, K. Nakabayashi, J. R. Shakirova, S. P. Tunik and S.-i. Ohkoshi, Neodymium β-diketonate showing slow magnetic relaxation and acting as a ratiometric thermometer based on near-infrared emission, *RSC Adv.*, 2019, **9**, 23444–23449.
15 A. A. Kitos, D. A. Gálico, N. Mavragani, R. Castañeda, J. O. Moilanen, J. L. Brusso and M. Murugesu, Probing optical and magnetic properties via subtle stereoelectronic effects in mononuclear DyIII-complexes, *Chem. Commun.*, 2021, **57**, 7818–7821.
16 R. A. S. Ferreira, E. Mamontova, A. M. P. Botas, M. Shestakov, J. Vanacken, V. Moshchalkov, Y. Guari, L. F. Chibotaru, D. Luneau, P. S. André, J. Larionova, J. Long and L. D. Carlos, Synchronous temperature and magnetic field dual-sensing by luminescence in a dysprosium single-molecule magnet, *Adv. Opt. Mater.*, 2021, **9**, 2101495.
17 J. Corredoira-Vázquez, C. González-Barreira, M. Fondo, A. M. García-Deibe, J. Sanmartín-Matalobos, M. A. Hernández-Rodríguez and L. D. Carlos, Luminescence thermometry in a Dy4 single molecule magnet, *Dalton Trans.*, 2022, **51**, 15593–15600.
18 S. Zanella, M. Aragon-Alberti, C. D. S. Brite, F. Salles, L. D. Carlos and J. Long, Luminescent single-molecule magnets as dual magneto-optical molecular thermometers, *Angew. Chem., Int. Ed.*, 2023, **62**, e202306970.
19 A. G. Bispo-Jr, L. Yeh, D. Errulat, D. A. Gálico, F. A. Sigoli and M. Murugesu, Improving the performance of β-diketonate-based Dy^{III} single-molecule magnets displaying luminescence thermometry, *Chem. Commun.*, 2023, **59**, 8723–8726.
20 R. Marin, D. A. Gálico, R. Gayfullina, J. O. Moilanen, L. D. Carlos, D. Jaque and M. Murugesu, A zero-field single-molecule magnet with luminescence thermometry capabilities containing soft donors, *J. Mater. Chem. C*, 2022, **10**, 13946–13953.
21 D. A. Gálico, R. Marin, G. Brunet, D. Errulat, E. Hemmer, F. A. Sigoli, J. O. Moilanen and M. Murugesu, Triplet-state position and crystal-field tuning in opto-magnetic lanthanide complexes: Two sides of the same coin, *Chem. – Eur. J.*, 2019, **25**, 14625–14637.
22 J. Wang, J. J. Zakrzewski, M. Zychowicz, V. Vieru, L. F. Chibotaru, K. Nakabayashi, S. Chorazy and S.-i. Ohkoshi, Holmium(III) molecular nanomagnets for optical thermometry exploring the luminescence re-absorption effect, *Chem. Sci.*, 2021, **12**, 730–741.
23 G. Brunet, R. Marin, M.-J. Monk, U. Resch-Genger, D. A. Gálico, F. A. Sigoli, E. A. Suturina, E. Hemmer and M. Murugesu, Exploring the dual functionality of an ytterbium complex for luminescence thermometry and slow magnetic relaxation, *Chem. Sci.*, 2019, **10**, 6799–6808.
24 M. Fondo, J. Corredoira-Vázquez, A. M. García-Deibe, J. Sanmartín-Matalobos, M. Amoza, A. M. P. Botas, R. A. S. Ferreira, L. D. Carlos and E. Colacio, Field-induced slow magnetic relaxation and luminescence thermometry in a mononuclear ytterbium complex, *Inorg. Chem. Front.*, 2020, **7**, 3019–3029.

25 K. Kumar, O. Stefanczyk, K. Nakabayashi, K. Imoto, Y. Oki and S.-i. Ohkoshi, Detection of sub-terahertz Raman response and nonlinear optical effects for luminescent Yb (III) complexes, *Adv. Opt. Mater.*, 2022, **10**, 2101721.

26 J. Wang, J. J. Zakrzewski, M. Heczko, M. Zychowicz, K. Nakagawa, K. Nakabayashi, B. Sieklucka, S. Chorazy and S.-i. Ohkoshi, Proton conductive luminescent thermometer based on near-infrared emissive $\{YbCo_2\}$ molecular nanomagnets, *J. Am. Chem. Soc.*, 2020, **142**, 3970–3979.

27 K. Karachousos-Spiliotakopoulos, V. Tangoulis, N. Panagiotou, A. Tasiopoulos, E. Moreno-Pineda, W. Wernsdorfer, M. Schulze, A. M. P. Botas and L. D. Carlos, Luminescence thermometry and field induced slow magnetic relaxation based on a near infrared emissive heterometallic complex, *Dalton Trans.*, 2022, **51**, 8208–8216.

28 V. Tangoulis, V. Nastopoulos, N. Panagiotou, A. Tasiopoulos, G. Itskos, M. Athanasiou, E. Moreno-Pineda, W. Wernsdorfer, M. Schulze and O. Malina, High-performance luminescence thermometer with field-induced slow magnetic relaxation based on a heterometallic cyanido-bridged 3d–4f complex, *Inorg. Chem.*, 2022, **61**, 2546–2557.

29 K. Karachousos-Spiliotakopoulos, V. Tangoulis, N. Panagiotou, A. Tasiopoulos, V. Nastopoulos, E. Moreno-Pineda, W. Wernsdorfer, M. Schulze, A. M. P. Botas and L. D. Carlos, Lanthanide luminescence thermometry and slow magnetic relaxation in 3-D polycyanidometallate-based materials, *Inorg. Chem.*, 2022, **61**, 18629–18639.

30 G. Félix, S. Sene, A. Kulakova, A. N. Bilyachenko, V. N. Khrustalev, E. S. Shubina, Y. Guari and J. Larionova, Tetranuclear lanthanide-based silsesquioxanes: Towards a combination of a slow relaxation of the magnetization and a luminescent thermometry, *RSC Adv.*, 2023, **13**, 26302–26312.

31 J. Wang, J. J. Zakrzewski, M. Zychowicz, Y. Xin, H. Tokoro, S. Chorazy and S.-i. Ohkoshi, Desolvation-induced highly symmetrical terbium(III) single-molecule magnet exhibiting luminescent self-monitoring of temperature, *Angew. Chem., Int. Ed.*, 2023, **62**, e202306372.

32 S. Ma, T. Zhang, J.-P. Zhao, Z.-Y. Liu and F.-C. Liu, A magnetic site dilution approach to achieve bifunctional fluorescent thermometers and single-ion magnets, *Dalton Trans.*, 2021, **50**, 1307–1312.

33 P.-Y. Liao, Y. Liu, Z.-Y. Ruan, H.-L. Wang, C.-G. Shi, W. Deng, S.-G. Wu, J.-H. Jia and M.-L. Tong, Magnetic and luminescent dual responses of photochromic hexaazamacrocyclic lanthanide complexes, *Inorg. Chem.*, 2023, **62**, 1075–1085.

34 J. Corredoira-Vázquez, P. Oreiro-Martínez, A. M. García-Deibe, J. Sanmartín-Matalobos and M. Fondo, A Dy^{III} complex of a pentadentate Schiff base with field-induced single-ion magnet behaviour, *Magnetochemistry*, 2023, **9**, 62.

35 M. Fondo, J. Corredoira-Vázquez, A. M. García-Deibe, J. Sanmartín-Matalobos, J. M. Herrera and E. Colacio, Designing ligands to isolate ZnLn and Zn_2Ln complexes: field-induced single-ion magnet behavior of the ZnDy, Zn_2Dy, and Zn_2Er analogues, *Inorg. Chem.*, 2017, **56**, 5646–5656.

36 M. Fondo, J. Corredoira-Vázquez, A. Herrera-Lanzós, A. M. García-Deibe, J. Sanmartín-Matalobos, J. M. Herrera, E. Colacio and C. Nuñez, Improving the SMM and luminescence properties of lanthanide complexes with LnO_9 cores in the presence of Zn^{II}: An emissive Zn_2Dy single ion magnet, *Dalton Trans.*, 2017, **46**, 17000–17009.

37 A. B. Canaj, S. Dey, E. R. Martí, C. Wilson, G. Rajaraman and M. Murrie, Insight into D_{6h} symmetry: Targeting strong axiality in stable dysprosium(III) hexagonal bipyramidal single-ion magnets, *Angew. Chem., Int. Ed.*, 2019, **58**, 14146–14151.

38 (*a*) M. Llunell, D. Casanova, J. Cirera, P. Alemany and S. Alvarez, *SHAPE, version 2.1*, Universitat de Barcelona, Barcelona, Spain, 2013; (*b*) A. Ruiz-Martínez, D. Casanova and S. Alvarez, Polyhedral structures with an odd number of vertices: Mine-coordinate metal compounds, *Chem. – Eur. J.*, 2008, **14**, 1291–1303; (*c*) M. Llunell, D. Casanova, J. Cirera, P. Alemany and S. Alvarez, *SHAPE: Program for the stereochemical analysis of molecular fragments by means of continuous shape measures and associated tools*, University of Barcelona, Barcelona, Spain, 2010.

39 J. Tang and P. Zhang, in *Lanthanide Single Molecule Magnets*, ed. J. Tang and P. Zhang, Springer, Berlin, Heidelberg, 2015, pp. 1–39.

40 J. Corredoira-Vázquez, C. González-Barreira, P. Oreiro-Martínez, A. M. García-Deibe, J. Sanmartín-Matalobos and M. Fondo, Lanthanoid complexes of pentadentate and hexadentate N_5 and N_6 macrocycles: synthesis and applications, *J. Rare Earths*, 2024, **42**, 1–15.

41 Y. Gil, R. C. de Santana, A. S. S. de Camargo, L. G. Merízio, P. F. Carreño, P. Fuentealba, J. Manzur and E. Spodine, Dual visible and near-infrared luminescence in mononuclear macrocyclic erbium(III) complexes via ligand and metal centred excitation, *Dalton Trans.*, 2023, **52**, 3158–3168.

42 A. N. Carneiro Neto, E. E. S. Teotonio, G. F. de Sá, H. F. Brito, J. Legendziewicz, L. D. Carlos, M. C. F. C. Felinto, P. Gawryszewska, R. T. Moura, R. L. Longo, W. M. Faustino and O. L. Malta, in *Handbook on the Physics and Chemistry of Rare Earths*, ed. J.-C. G. Bünzli and V. K. Pecharsky, Elsevier, 2019, vol. 56, pp. 55–162.

43 A. N. Carneiro Neto, E. Mamontova, A. M. P. Botas, C. D. S. Brites, R. A. S. Ferreira, J. Rouquette, Y. Guari, J. Larionova, J. Long and L. D. Carlos, Rationalizing the thermal response of dual-center molecular thermometers: The example of an Eu/Tb coordination complex, *Adv. Opt. Mater.*, 2022, **10**, 2101870.

44 E. Kasprzycka, A. N. Carneiro Neto, V. A. Trush, L. Jerzykiewicz, V. M. Amirkhanov, O. L. Malta, J. Legendziewicz and P. Gawryszewska, How minor structural changes generate major consequences in photo-

physical properties of RE coordination compounds; Resonance effect, LMCT state, *J. Rare Earths*, 2020, **38**, 552–563.

45 J. Manzur, P. Fuentealba, Y. Gil, J. Pérez-Obando, J. Morales Alfaro, A. I. Vega Carvallo, D. Aravena, R. C. d. Santana, A. N. Carneiro Neto and E. Spodine, Tuning the emission of homometallic Dy^{III}, Tb^{III}, and Eu^{III} 1-D coordination polymers with 2,6-di(1H-1,2,4-triazole-1-yl-methyl)-4-*R*-phenoxo ligands: Sensitization through the singlet state, *Inorg. Chem.*, 2023, **62**, 19195–19207.

46 R. T. Moura Jr., J. A. Oliveira, I. A. Santos, E. M. de Lima, L. D. Carlos, E. C. Aguiar and A. N. C. Neto, Theoretical evidence of the singlet predominance in the intramolecular energy transfer in Ruhemann's purple Tb(III) complexes, *Adv. Theory Simul.*, 2021, **4**, 2000304.

47 S. Chorazy, M. Rams, K. Nakabayashi, B. Sieklucka and S.-i. Ohkoshi, White light emissive DyIII single-molecule magnets sensitized by diamagnetic [CoIII(CN)6]3− linkers, *Chem. – Eur. J.*, 2016, **22**, 7371–7375.

48 A. Bednarkiewicz, L. Marciniak, L. D. Carlos and D. Jaque, Standardizing luminescence nanothermometry for biomedical applications, *Nanoscale*, 2020, **12**, 14405–14421.

49 C. D. S. Brites, P. P. Lima, N. J. O. Silva, A. Millán, V. S. Amaral, F. Palacio and L. D. Carlos, Thermometry at the nanoscale, *Nanoscale*, 2012, **4**, 4799–4829.

50 C. D. S. Brites, A. Millán and L. D. Carlos, in *Handbook on the physics and chemistry of rare earths*, ed. B. Jean-Claude and P. Vitalij K, Elsevier, 2016, vol. 49, pp. 339–427.

51 J. C. Martins, C. D. S. Brites, A. N. C. Neto, R. A. S. Ferreira and L. D. Carlos, *An overview of luminescent primary thermometers*, Springer International Publishing, Cham, 2023.

52 J. C. Martins, A. R. N. Bastos, R. A. S. Ferreira, X. Wang, G. Chen and L. D. Carlos, Primary luminescent nanothermometers for temperature measurements reliability assessment, *Adv. Photonics Res.*, 2021, **2**, 2000169.

53 S. Balabhadra, M. L. Debasu, C. D. S. Brites, R. A. S. Ferreira and L. D. Carlos, Upconverting nanoparticles working as primary thermometers in different media, *J. Phys. Chem. C*, 2017, **121**, 13962–13968.

54 F. E. Maturi, A. Gaddam, C. D. S. Brites, J. M. M. Souza, H. Eckert, S. J. L. Ribeiro, L. D. Carlos and D. Manzani, Extending the palette of luminescent primary thermometers: Yb3+/Pr3 + co-doped fluoride phosphate glasses, *Chem. Mater.*, 2023, **35**, 7229–7238.

55 C. D. S. Brites, E. D. Martínez, R. R. Urbano, C. Rettori and L. D. Carlos, Self-calibrated double luminescent thermometers through upconverting nanoparticles, *Front. Chem.*, 2019, **7**, 267.

56 G. M. Sheldrick, *SADABS, area-detector absorption correction*, Siemens Industrial Automation, Inc., Madison, WI, 2007.

57 G. Sheldrick, SHELXT - Integrated space-group and crystal-structure determination, *Acta Crystallogr., Sect. A: Found. Adv.*, 2015, **71**, 3–8.

58 G. M. Sheldrick, Crystal structure refinement with SHELXL, *Acta Crystallogr., Sect. C: Struct. Chem.*, 2015, **71**, 3–8.

